Epistemic uncertainty quantification for Reynolds-averaged Navier-Stokes modeling of separated flows over streamlined surfaces ⓔⓟ

C. Gorlé, S. Zeoli, M. Emory, J. Larsson, and G. Iaccarino

COLLECTIONS

ⓔⓟ   This paper was selected as an Editor's Pick

View Online   Export Citation   CrossMark

Epistemic uncertainty quantification for Reynolds-averaged Navier-Stokes modeling of separated flows over streamlined surfaces (EP)

C. Gorlé,[1,a),b)] S. Zeoli,[2] M. Emory,[3,b)] J. Larsson,[4,b)] and G. Iaccarino[5]

AFFILIATIONS

[1] Civil and Environmental Engineering Department, Stanford University, Stanford, California 94305, USA
[2] Department of Mechanical Engineering, University of Mons, Mons, Belgium
[3] Cascade Technologies, Inc., Palo Alto, California 94303, USA
[4] Department of Mechanical Engineering, University of Maryland, College Park, Maryland 20742, USA
[5] Center for Turbulence Research, Stanford University, Stanford, California 94305, USA

[a)] **Electronic mail:** gorle@stanford.edu.
[b)] At the Center for Turbulence Research when this work was initiated.

ABSTRACT

It is well known that linear eddy-viscosity turbulence models can introduce uncertainty in predictions for complex flow features such as separation and reattachment. The goal of this paper is to advance our understanding of a physics-based approach to quantify this turbulence model form uncertainty in Reynolds-averaged Navier-Stokes simulations of separated flows over streamlined surfaces. The methodology is based on perturbing the modeled Reynolds stresses in the momentum equations; perturbations are defined in terms of a decomposition of the Reynolds stress tensor, i.e., based on the tensor magnitude and the eigenvalues and eigenvectors of the normalized anisotropy tensor. We demonstrate that the accuracy of the predicted Reynolds stress magnitude is strongly influenced by the turbulence production term and subsequently explore the anisotropy tensor eigenvalue and eigenvector perturbations that maximize or minimize turbulence production; these could be expected to provide bounds on the prediction of separation and reattachment locations. The method uses two user-defined parameters to identify the spatial extent of the perturbed region and the magnitude of the eigenvalue perturbations. Results for the flow over a periodic wavy wall and over a three-dimensional hill indicate that the perturbations that increase turbulence production decrease the extent of the separation region, while perturbations that decrease production increase the region of separated flow. The predicted bounds can successfully encompass the reference data, provided the extent of the perturbed region and the eigenvalue perturbation magnitudes are sufficiently large. Importantly, we observed a monotonic behavior of the magnitude of the predicted bounds as a function of the two user-defined parameters.

Published under license by AIP Publishing. https://doi.org/10.1063/1.5086341

I. INTRODUCTION

While Reynolds-averaged Navier-Stokes (RANS) simulations remain the most affordable technique for simulating turbulent flows, the inability of linear eddy-viscosity models to consistently provide accurate predictions for complex flow features such as separation and reattachment is a well known limitation of the approach. Large-eddy simulations (LES) provide a higher-fidelity solution for such flow problems, but they come at a significant increase in computational time and cost, in particular, for high-Reynolds number flows. Hence, the engineering practice would benefit from a methodology to quantify the structural uncertainty in RANS models. More expensive LES would then only be necessary if that uncertainty is too large.

Previous studies have considered a variety of approaches toward epistemic uncertainty quantification of turbulence models, including Bayesian inference,[1] adjoint methods,[2]

and machine learning.[3–10] In the present study, we consider the approach introduced by Emory, Larsson, and Iaccarino,[11] which quantifies the uncertainty related to the turbulence model through the introduction of perturbations in the Reynolds stress tensor computed by the baseline model. The perturbations are defined in terms of the tensor magnitude (turbulence kinetic energy), and the shape (eigenvalues) and orientation (eigenvectors) of the normalized anisotropy tensor. Initial work focused on the effect of eigenvalue perturbations, exploring the bounds obtained by making the turbulence more one-, two-, or three-component.[11] Several follow-up studies have further developed this approach. On the one hand, a variety of data-driven methods have been proposed to define the perturbations, some also considering perturbations to the magnitude and orientation of the Reynolds stress tensor.[4,6,8,9,12] On the other hand, a physics-based extension toward perturbing the magnitude and orientation has been proposed.[13,14] In contrast to the data-driven methods, this approach requires no high-fidelity data input and was formulated to be generally applicable. It consists of indirectly perturbing the magnitude of the Reynolds stress tensor by calculating the production term in the transport equation for the turbulence kinetic energy using the perturbed normalized anisotropy tensor. The tensor eigenvalue and eigenvector perturbations are selected to minimize and maximize the production term since this can be expected to provide bounds on predictions for separation and reattachment points. In the study by Gorlé et al.,[13] an analysis for the flow over a wavy wall indicated that maximum production is found for perturbations to the one-component corner of the barycentric map without rotation of the eigenvectors. Isotropic turbulence, which eliminates production of turbulence kinetic energy, was considered the minimum production scenario. These perturbations produced bounds on the predicted separation and reattachment points in the flow over a wavy wall that encompassed direct numerical simulation (DNS) data.[15] In the study by Iaccarino, Mishra, and Ghili,[14] it was mathematically confirmed that for any set of realizable eigenvalues, production is maximized when using the eigenvectors of the rate of strain tensor, while the minimum is found when switching the first and third eigenvector of the rate of strain tensor. Similar to Gorlé et al.,[13] results were presented for eigenvalue perturbations to the one-component corner of the map without rotation, and to the isotropic corner, where the orientation of the eigenvectors has no influence on the solution. The results further demonstrated the promising capabilities of the approach in different 2D and axi-symmetric flow configurations.

The goal of this paper is to advance the understanding of the performance of this physics-based approach for quantifying linear eddy-viscosity turbulence model form uncertainty in RANS simulations of separated flows over streamlined surfaces. Specifically, the objectives of this study are (1) to support the choice of indirectly perturbing the turbulence kinetic energy by calculating the production term with the perturbed anisotropy tensor; (2) to mathematically demonstrate that eigenvalue perturbations to one-component turbulence without eigenvector perturbations achieve maximum production, while isotropic turbulence is the limiting case when restricting the solution to positive production; (3) to investigate the behavior of the bounds obtained using these one-component and isotropic perturbations in function of the magnitude and spatial extent of the perturbations; and (4) to apply the method to a complex three-dimensional flow of engineering interest. To achieve the first three objectives, we revisit the test case of the flow over a wavy wall used in the study by Gorlé et al.[13] A DNS database for the configuration[15] is used to support validation of the methodology. For the fourth objective, we consider the flow over Askervein Hill, which is a test case of interest for wind resource assessment, and we compare the results to field experiments.[16,17]

The remainder of this paper is organized as follows. Section II introduces the governing equations and the flow configurations considered. Section III addresses the first two objectives by presenting a detailed description and motivation of the method used to define the perturbations. Sections IV and V present the results for both configurations, addressing the final two objectives. Conclusions are presented in Sec. VI.

II. GOVERNING EQUATIONS AND FLOW CONFIGURATIONS

A. Governing equations

The governing equations are the incompressible Reynolds-averaged equations for conservation of mass and momentum,

$$\frac{\partial U_i}{\partial x_i} = 0, \tag{1}$$

$$\frac{DU_j}{Dt} = -\frac{1}{\rho}\frac{\partial p}{\partial x_j} + \nu \frac{\partial^2 U_j}{\partial x_i \partial x_i} - \frac{\partial \overline{u_i u_j}}{\partial x_i}, \tag{2}$$

where U_i are the time-averaged velocity components, ρ is the density, p is the pressure, and ν is the kinematic viscosity. $\overline{u_i u_j}$ are the components of the Reynolds stress tensor R_{ij}, which are modeled with a two-equation linear eddy viscosity model based on the turbulent viscosity hypothesis,

$$\overline{u_i u_j} = \frac{2}{3}k\delta_{ij} - 2\nu_t S_{ij}, \tag{3}$$

where k is the turbulence kinetic energy, δ_{ij} is the Kronecker delta, ν_t is the turbulent viscosity, and S_{ij} is the rate of strain tensor. In the results presented hereafter for the wavy wall, two different models for the turbulent viscosity were considered: the shear-stress transport $k - \omega$ model (SST) and the realizable $k - \epsilon$ model (RKE). By considering two different models, we intend to demonstrate that the approach consistently provides bounds for the prediction, independent of the choice for the baseline model. For the Askervein hill case, the SST $k - \omega$ model was used.

B. Wavy wall configuration and DNS database

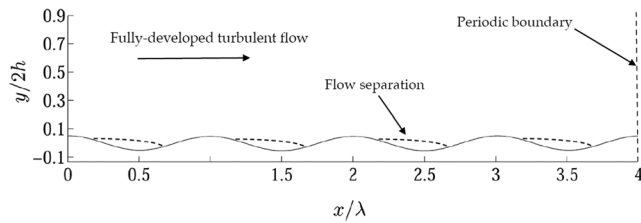The wavy wall configuration, shown in Fig. 1, is identical to the one from the DNS study used for validation.[15]

FIG. 1. Wavy wall flow configuration.[15]

The geometry is defined as a three-dimensional channel, with a flat upper wall and a wavy surface at the lower wall defined by

$$y = A \cos\left(\frac{2\pi x}{\lambda}\right), \qquad (4)$$

with A being the amplitude and λ being the wavelength. The wave steepness is defined by $2A/\lambda$ and equal to 0.1. Periodic boundary conditions are applied in the streamwise direction. The RANS simulations were performed on a mesh of 256×96 cells. This mesh resolution is identical to the one used in the DNS[15] and can hence be presumed to provide a grid independent solution. The near wall resolution was sufficient ($y^+ \approx 1$) to avoid the use of wall functions with the SST $k - \omega$ model; with the realizable $k - \epsilon$ model a two-layer approach was used.[18]

The governing equations presented in Sec. II A are solved using an unstructured, pressure-based, finite-volume code. The solver uses a co-located scheme, interpolating the pressure values at the faces with a standard algorithm.[19] Pressure-velocity coupling is performed using the semi-implicit method for pressure-linked equations (SIMPLE) algorithm.[20] A second order upwind scheme is used for spatial discretization, and the gradients are evaluated with a Green-Gauss cell based approach. The solution is considered converged when the residuals level out and no change in the solution is observed.

The DNS database includes results for the flow and for scalar dispersion at $Re = 6850$, based on the bulk velocity U_b at the wave crest and the average channel height h. The present study focuses on the solution for the flow field, in particular, on the Reynolds stress tensor obtained from the time-averaged DNS solution. Validation of the DNS flow field is presented in Rossi.[21] The time-averaged values used in this study were also spatially averaged in the spanwise direction and over the four wave crests since the flow is assumed to be fully developed and hence periodic in both directions.

C. Askervein hill configuration and field measurements

The geometry of Askervein hill, an isolated 116 m high hill near the west coast of South Uist, Scotland, is shown in Fig. 2. The location was selected for a field experiment performed in September 1982 and October 1983,[16,17] and the data have been widely used for validation of experimental and numerical methods in the wind engineering community. RANS
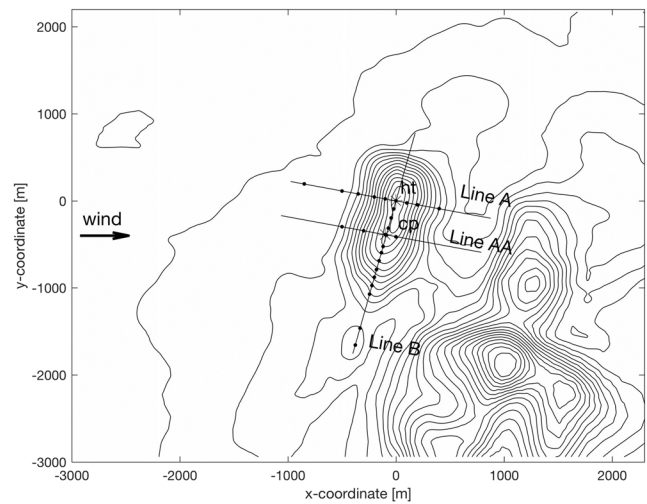

FIG. 2. Computational domain and topography of the Askervein hill and its surroundings.

simulations using the standard and RNG $k - \epsilon$ turbulence models[22–26] are generally found to predict mean flow quantities in agreement with the measurements, but they tend to underestimate the relative speed-up near the ground at the hilltop. This underestimation has been attributed to the presence of the intermittent separation in the lee of the hill or to the hilltop area being slightly smoother than the upstream terrain. In the present study, we investigate whether turbulence model form uncertainty could be responsible for the observed discrepancies.

The RANS simulations were performed with the SST $k - \omega$ turbulence model for an incoming wind direction of $210°$, aligned with the x-axis of the computational model, as presented in Fig. 2. The horizontal extent of the computational domain is shown in Fig. 2, and the height is 1800 m. The computational grid has around 2×10^6 cells and is refined in the near wall region to accurately resolve the geometry of the hill. A previously reported grid dependency study indicated negligible changes in the predicted quantities of interest when increasing the grid resolution by a factor 1.5.[27] The inflow boundary condition imposes neutral atmospheric boundary layer profiles,[28] with a logarithmic velocity profile that has a roughness height $z_0 = 0.03$ m[16] and a friction velocity $u_* = 0.63$ m/s to match the velocity measurements at a reference tower. A rough wall function is used to ensure horizontal homogeneity of the atmospheric boundary layer profiles.[29] At the top boundary, a zero normal velocity is imposed, while zero-gradient conditions are used for all velocity components on the outlet boundary.

The governing equations presented in Sec. II A are solved using the open source unstructured, pressure-based, finite-volume code OpenFoam. Pressure-velocity coupling is performed using the SIMPLE algorithm,[20] and a central differencing scheme is used for spatial discretization of the convective terms. The solution is considered converged when

the residuals level out and no change in the solution is observed.

Experimental data for validation are available at several points on lines A, AA, and B at a height of 10 m above the hill surface, as indicated in Fig. 2. The analysis of the results will focus on the prediction of the fractional speed-up ratio, FSR = $(U - U_{ref})/U_{ref}$, with U_{ref} being the incoming wind speed at 10 m height equal to 8.9 m/s.

III. EPISTEMIC UNCERTAINTY QUANTIFICATION METHOD

A. General framework

The framework proposed in the study by Emory, Pecnik, and Iaccarino[30] consists in perturbing the Reynolds stress tensor R_{ij} computed by the model and used in the momentum equations. The definition of the perturbed tensor R_{ij}^* is based on the eigenvalue decomposition of the normalized anisotropy tensor $a_{ij} = \frac{R_{ij}}{2k} - \frac{1}{3}\delta_{ij} = v_{ik}\Lambda_{kl}v_{jl}$, where v_{ij} is the matrix of orthonormal eigenvectors and Λ_{kl} is the diagonal matrix of eigenvalues λ_l,

$$R_{ij}^* = 2k^* \left(\frac{1}{3}\delta_{ij} + v_{ik}^* \Lambda_{kl}^* v_{jl}^* \right). \tag{5}$$

Here, k^* is the perturbed turbulence kinetic energy, Λ_{kl}^* is the diagonal matrix of perturbed eigenvalues λ_l^*, and v_{ij}^* are the perturbed eigenvectors. The above formulation does not involve any modeling assumptions, thereby presenting a general way of introducing epistemic uncertainty in the Reynolds stress tensor. In the following, we first present the rationale for defining perturbations to the turbulence kinetic energy and subsequently focus on the perturbations for the anisotropy tensor.

1. Perturbation of turbulence kinetic energy

The proposed approach does not perturb k directly but instead perturbs the production term in the transport equation for k. The production of k can be written in closed form as the inner product of the Reynolds stresses and the rate of strain tensor, $P_k = -\overline{u_i u_j}\frac{\partial U_i}{\partial x_j}$. Hence, the approach can leverage the perturbations introduced in the eigenvalues and the eigenvectors in Eq. (5), by using the perturbed anisotropy tensor in the exact formulation for P_k.

This modeling choice is based on an analysis of the discrepancies in k between the RANS and DNS simulations for the wavy wall. Three different sets of simulations were performed. First, both the RANS flow and turbulence equations were solved. Second, the effect of the coupling to the mean flow was eliminated by freezing the flow to the averaged DNS flow field, solving the transport equations for the turbulence quantities, k and ω or ϵ only. Third, the turbulence kinetic energy production term was also frozen to the exact production term calculated from the DNS as $P_k = -\overline{u_i u_j}\frac{\partial U_i}{\partial x_j}$. The difference between the last two sets of simulations is that when only freezing the DNS flow field, P_k is still determined from the inexact Reynolds stresses as computed using the linear eddy-viscosity hypothesis, whereas in the second case, the exact Reynolds stresses are used.

Figure 3 presents the comparison for the turbulence kinetic energy from the DNS and from the three different simulations with the SST $k - \omega$ and the realizable $k - \epsilon$ models. For the SST $k - \omega$ model, the result shows an underprediction up to 70% when solving the coupled momentum and turbulence transport equations. When removing the coupling to the mean flow, the turbulence kinetic energy decreases further, increasing the level of discrepancy. However, when using the correct production term for k, a much higher accuracy in the prediction is obtained, with a prediction that is closer to the DNS in most regions of the flow than the original coupled RANS solution. For the $k - \epsilon$ model, an overprediction up to 40% is observed when solving the coupled momentum and turbulence transport equations. When removing the coupling to the mean flow, the overprediction increases up to 100%. As for the
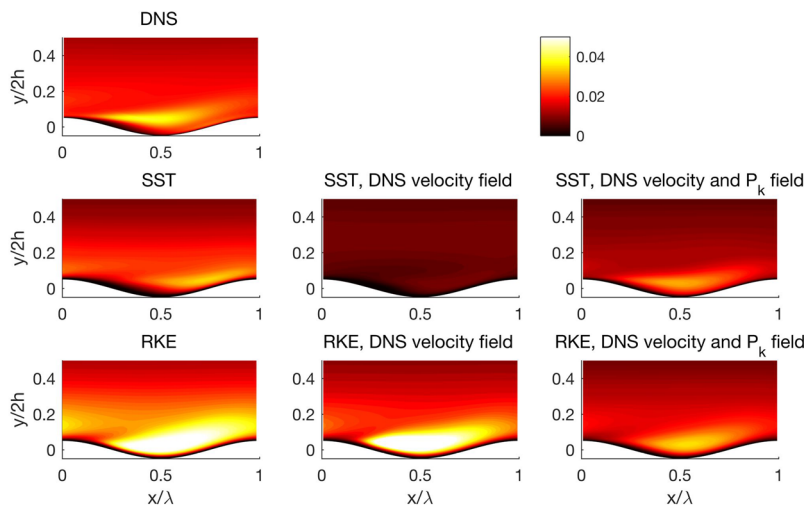

FIG. 3. Comparison of turbulence kinetic energy for the flow over the wavy wall. DNS and RANS with the SST $k - \omega$ and realizable $k - \epsilon$ models, solving the coupled momentum and turbulence transport equations (left), solving the turbulence transport equations with the DNS mean flow field (center), and solving the turbulence transport equations with the DNS mean flow field and DNS production term for k (right).

SST $k - \omega$ model, imposing the correct production term for k results in an improvement of the prediction, with a result that is close to the original coupled RANS solution.

These results demonstrate that the use of the original model's Reynolds stress prediction to calculate P_k is an important reason for errors in the prediction of the turbulence kinetic energy, hence motivating our approach for perturbing the production term. In addition, this approach allows us to explore which anisotropy tensor perturbations would minimize and maximize P_k. These perturbations could plausibly provide realistic bounds for RANS predictions of separated flows over a streamlined surface.

2. Perturbation of eigenvalues and eigenvectors

Perturbations of the eigenvectors can be defined in terms of a rotation of the principal axes of the anisotropy tensor. For the eigenvalues, Emory, Pecnik, and Iaccarino[30] proposed perturbations defined as a modification of the barycentric map[31] coordinates. The method imposes clear bounds on the possible perturbations since the map, shown in Fig. 4, contains all the realizable states of the Reynolds stress tensor. Its corners represent different limiting states of turbulence anisotropy; these are referred to by their corresponding number of components, e.g., isotropic turbulence corresponds to the three-component (3C) corner. The barycentric map coordinates for any Reynolds stress tensor are determined by a linear combination of the corner coordinates x_{iC} and the anisotropy tensor eigenvalues, $\lambda_1 \geq \lambda_2 \geq \lambda_3$,

$$\mathbf{x} = (\lambda_1 - \lambda_2)\mathbf{x}_{1C} + (2\lambda_2 - 2\lambda_3)\mathbf{x}_{2C} + (3\lambda_3 + 1)\mathbf{x}_{3C}. \quad (6)$$

The procedure to define the perturbed eigenvalues λ_l^* is to first determine the map coordinates of the Reynolds stress computed by the SST $k - \omega$ or realizable $k - \epsilon$ turbulence model x_A and subsequently inject uncertainty by moving it to a new location x_B. For example, when the perturbations are intended to make the anisotropy tensor more one-component, x_B can be written as

$$\mathbf{x_B} = \mathbf{x_A} + \Delta B(\mathbf{x_{1C}} - \mathbf{x_B}), \quad (7)$$

where ΔB is the magnitude of the perturbation toward the 1C corner. Once the new location has been determined, an updated set of eigenvalues λ_l^* can be evaluated from Eq. (6) and used to reconstruct a_{ij} and the Reynolds stress tensor. Given this framework, our objective is now to find the eigenvalue and eigenvector perturbations that produce the maximum and minimum turbulence production term.

a. Maximizing the production of k. It has been shown that the production term, which is the inner product of the Reynolds stress tensor and the rate of strain tensor, has the following minimum and maximum:[14]

$$[\rho_1\gamma_3 + \rho_2\gamma_2 + \rho_3\gamma_1, \rho_1\gamma_1 + \rho_2\gamma_2 + \rho_3\gamma_3], \quad (8)$$

where $\rho_1 \geq \rho_2 \geq \rho_3$ are the eigenvalues of the Reynolds stress tensor and $\gamma_1 \geq \gamma_2 \geq \gamma_3$ are the eigenvalues of the rate of strain tensor. Thus, for a given set of eigenvalues, the maximum production term is found when the eigenvectors of the Reynolds stress tensor are equal to those of the rate of strain tensor. Given the turbulent viscosity hypothesis [Eq. (3)], this corresponds to the original orientation predicted by the realizable $k - \epsilon$ and SST $k - \omega$ models.

Next, we show that among the possible sets of eigenvalues, the ones corresponding to the one-component corner of the barycentric map consistently maximize the production term. First, the eigenvalues of the Reynolds stress tensor in Eq. (8) are written in terms of the eigenvalues of the anisotropy tensor, $\rho_j = \frac{2}{3}k + 2k\lambda_j$, showing that finding the maximum production is equivalent to finding the maximum of $\lambda_1\gamma_1 + \lambda_2\gamma_2 + \lambda_3\gamma_3$. Then, we substitute $\lambda_3 = -\lambda_1 - \lambda_2$, based on the fact that the anisotropy tensor has a zero trace, and we use $\gamma_2 = \gamma_1 - \epsilon$ and $\gamma_3 = \gamma_1 - \epsilon - \eta$, with $\epsilon, \eta \geq 0$, based on the ordering of the eigenvalues. This results in the equivalent optimization problem

$$\max. \lambda_1(\epsilon + \eta) + \lambda_2\eta, \quad (9)$$

subject to the linear constraints depicted in the anisotropy invariant map in Fig. 4. The solution for this linear optimization problem will correspond to one of the vertices in the invariant map. Substituting these limiting sets of eigenvalues, it is shown that the solution for this optimization problem is found in the one-component limit, when $\lambda_1 = \frac{2}{3}$ and $\lambda_2 = -\frac{1}{3}$. Hence, the production term will be maximized by introducing eigenvalue perturbations to the one-component corner in the barycentric map while keeping the eigenvectors aligned with those of the rate of strain tensor.
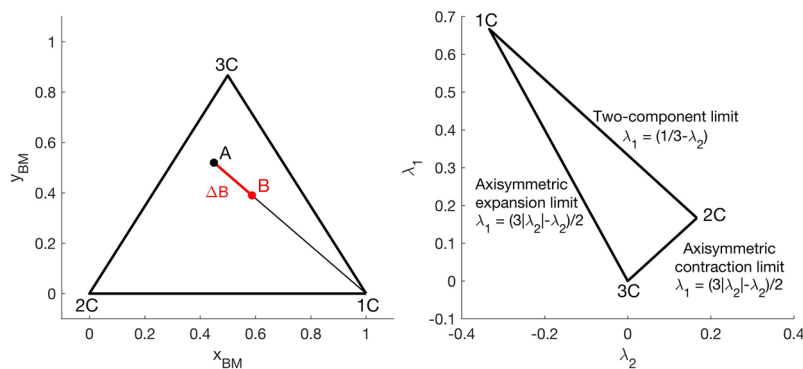

FIG. 4. Barycentric (left) and anisotropy-invariant (right) maps.

b. Minimizing the production of k. Following Eq. (8), minimum production is found when the eigenvectors of the rate of strain tensor are those of the Reynolds stress tensor but with the first and third eigenvector interchanged. Repeating the above analysis to find the eigenvalues that will produce the minimum production term for this orientation, we obtain the following equivalent for the optimization problem from Eq. (9):

$$\text{min.} - \lambda_1(\epsilon + \eta) - \lambda_2 \epsilon, \qquad (10)$$

again subject to the linear constraints depicted in the anisotropy invariant map in Fig. 4. In this case, we see that for isotropic turbulence, when $\lambda_1 = \lambda_2 = \lambda_3 = 0$, this relationship is 0, while for any other realizable set of eigenvalues, a negative production term would be obtained. Negative shear production has never been observed on an entire flow domain; it has only been observed locally in, e.g., asymmetric flow with one smooth and one rough wall, flow through annuli, wall jets, and asymmetric plane jets.[32] It is very unlikely to occur in the steady-state, non-buoyant flows over streamlined surfaces considered in this paper, and the DNS value for the shear production term was confirmed to be positive at all locations in the wavy wall flow field. Accessing negative turbulence production is therefore undesirable; instead we will consider eigenvalue perturbations to the isotropic corner in the barycentric map, which consistently decrease the turbulence kinetic energy. In the isotropic limit, the anisotropy tensor is a null tensor, and any rotation of the eigenvectors will have no influence on the result.

B. User-defined parameters

The introduction of eigenvalue perturbations to the 1C and 3C corners in the entire flow domain is likely to lead to overly conservative bounds on the prediction. We therefore introduce two user-defined parameters, specifying (1) the size of the flow region in which to introduce the perturbations and (2) the magnitude of the eigenvalue perturbation. In Secs. III B 1 and III B 2, the physical basis for the selection of these parameters is discussed; the effect of their values on the solution is investigated in Secs. IV and V.

1. Size of the perturbed flow region

To identify the regions in the flow where the results from the linear-eddy viscosity model are plausibly inaccurate, we use the marker function that was presented in the study by Gorlé et al.[33] The marker m identifies regions that deviate from parallel shear flow based on the angle between the local direction of the streamline s_i and the gradient of the streamline-aligned velocity g_j,

$$s_i = \frac{U_i}{\sqrt{U_k U_k}}, \qquad g_j = s_i \frac{\partial U_i}{\partial x_j}, \qquad m = |g_j s_j|, \qquad (11)$$

where m will be exactly zero for either parallel shear flow or when the shear vanishes. As the angle between the streamline and the gradient decreases, the magnitude of m will increase. In the study by Gorlé et al.,[33] the performance of

the marker was validated for the wavy wall flow by comparing the marker values with a local measure of the turbulence model error, defined as the difference between the divergence of the Reynolds stresses in the RANS and DNS solution.

To identify the regions in which Reynolds stress perturbations are introduced, upper and lower marker thresholds, M_u and M_l, are specified. These thresholds are used to define a switch function that varies between 0 and 1,

$$Switch = \begin{cases} 0 & \text{if } m < M_l, \\ \frac{1}{2} - \frac{1}{2}\cos\left(\pi \frac{m - M_l}{M_u - M_l}\right) & \text{if } M_l \le m \le M_u, \\ 1 & \text{if } m > M_u. \end{cases} \qquad (12)$$

The cosine function ensures a smooth transition, and the thresholds are specified in terms of the ratio between a reference length and reference velocity, U_{ref}/L_{ref}. Different combinations of M_l and M_u, summarized in Table I, were considered in this study. In Secs. IV and V, the corresponding contours for the switch functions obtained for both test cases will be shown to visualize the variation in the extent of the marked regions.

2. Magnitude of the eigenvalue perturbations

The magnitude of the perturbations toward the 1C and 3C corner of the barycentric map was restricted to movements that would bound the DNS value of the shear production term integrated over the domain. This was found to happen for both models when considering a maximum displacement that goes halfway to the corners of the map, i.e., using $\Delta B = 0.5$. Table II presents these integrated values normalized by the DNS value. To visualize the resulting perturbations of P_k, Fig. 5 shows the contours of the turbulence production term from the DNS, the unperturbed RANS model, and the RANS model with the perturbations that decrease (3C, $\Delta B = 0.5$) and increase (1C, $\Delta B = 0.5$) P_k. The results confirm that limiting the eigenvalue perturbations to $\Delta B = 0.5$ provides realistic perturbations for which the integrated values of the production term encompass the DNS value for both models.

TABLE I. Marker threshold values.

	M_l	M_u
M1	$0.05 U_{ref}/L_{ref}$	$0.1 U_{ref}/L_{ref}$
M2	$0.1 U_{ref}/L_{ref}$	$0.25 U_{ref}/L_{ref}$
M3	$0.25 U_{ref}/L_{ref}$	$0.5 U_{ref}/L_{ref}$

TABLE II. Turbulence production term, integrated over the domain and divided by the DNS value, for the unperturbed RANS simulations and for simulations with perturbations that increase (1C) and decrease (3C) P_k.

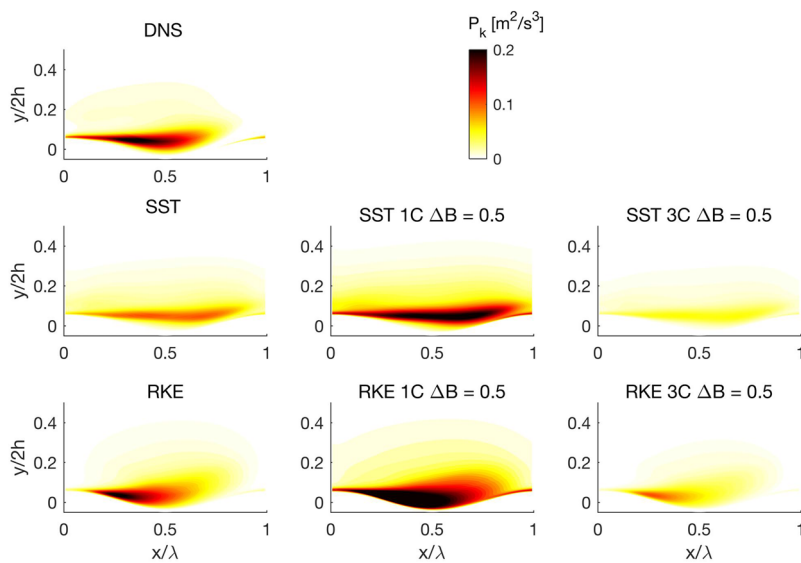|	$\frac{P_k}{P_{k,DNS}}$	$\frac{P_{k,1C,\Delta B=0.5}}{P_{k,DNS}}$	$\frac{P_{k,3C,\Delta B=0.5}}{P_{k,DNS}}$
SST $k - \omega$	0.95	2.06	0.47
Realizable $k - \epsilon$	1.02	2.53	0.51

FIG. 5. Contours of turbulence production for the wavy wall flow. DNS and unperturbed RANS using the SST $k - \omega$ and realizable $k - \epsilon$ models (left), and SST $k - \omega$ and realizable $k - \epsilon$ with perturbations that increase (center) and decrease (right) P_k.

C. Implementation

The implementation of the methodology is straightforward since it only requires specifying source terms in the momentum equations and the transport equation for the turbulence kinetic energy. The source terms are calculated at each iteration by (1) calculating the marker, (2) calculating the Reynolds stress tensor obtained by the baseline model, but using a source term that calculates the production of k using the perturbed tensor from the previous time step, (3) obtaining the normalized anisotropy tensor eigenvalue decomposition and barycentric map coordinates, (4) perturbing the barycentric map coordinates as proposed above and reconstructing the perturbed tensor, and (5) calculating the divergence of the perturbed tensor to define the source terms in the momentum equations. The iterative solver is initialized using the unperturbed solution and runs until it converges to the perturbed solution.

IV. WAVY WALL RESULTS AND DISCUSSION

In this section, we present the results obtained for the wavy wall configuration, focusing on the prediction of the wall shear stress and the velocity field. We consider both the SST and RKE turbulence models. The effect of the user-defined parameter values is investigated by performing a total of nine simulations, considering all possible combinations of the three marker thresholds (Table I) and three perturbation magnitudes ($\Delta B = 0.1, 0.25, 0.5$). The extent of the marked regions for each set of marker thresholds is shown in Fig. 6; these contours were calculated using the baseline SST and RKE solutions. Using both turbulence models, M1 results in introducing perturbations into most of the lower quarter of the channel, while for M3, perturbations will only be introduced in the near-wall regions.

A. Wall shear stress

Figure 7 presents the results in terms of the x-component of the wall shear stress along the wavy wall. Each plot includes the values from the DNS, a baseline RANS simulation (SST on the left, RKE on the right), and three sets of bounds, obtained from simulations with perturbations toward the one-component and three-component corner. In the upper row, the three different bounds reflect the effect of the
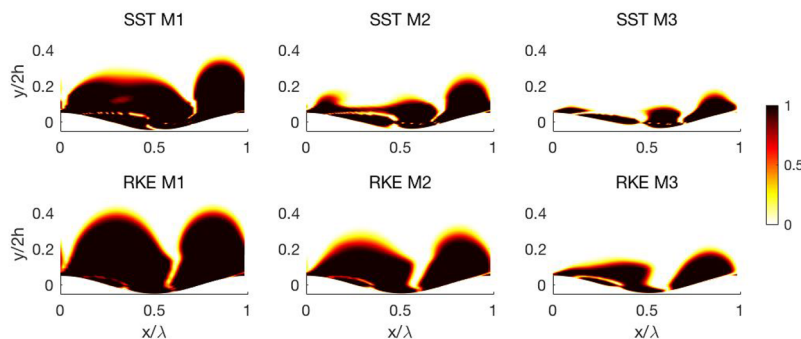

FIG. 6. Switch functions for marker thresholds M1, M2, and M3 in the SST and RKE simulations for the wavy wall.
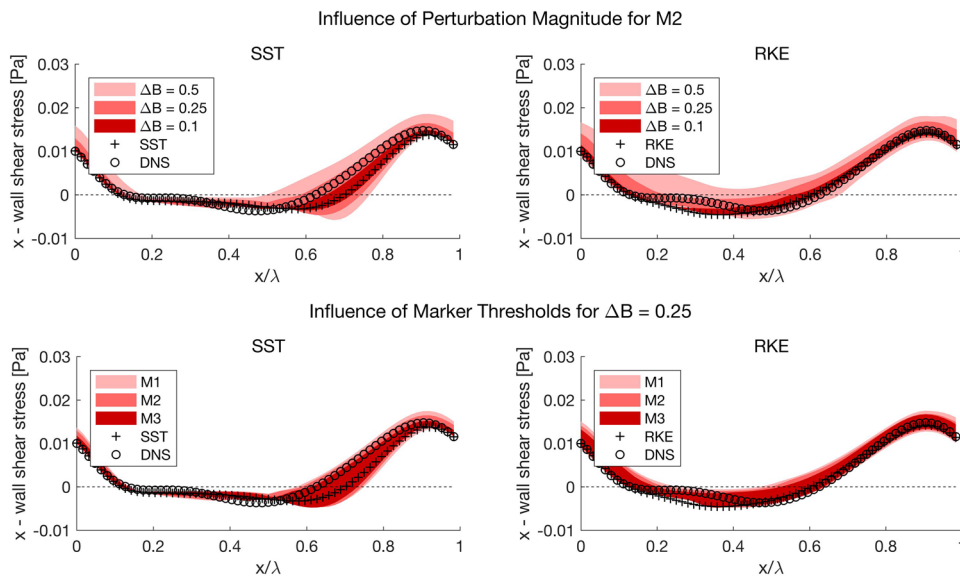
FIG. 7. Uncertainty intervals for the streamwise component of the wall shear stress along the wavy wall.

perturbation magnitude ΔB, shown for M2. The lower row demonstrates the effect of the extent of the marked region, shown for ΔB = 0.25.

The results show the promising capabilities of the approach in capturing the uncertainty in the reattachment location. The baseline SST prediction considerably over predicts the reattachment location, while the RKE model provides a rather accurate prediction, with a reattachment point that is only slightly upstream of the DNS result. As expected, the 3C perturbation, which decreases P_k, shifts the

reattachment point slightly downstream, while the 1C perturbation, which increases P_k, shifts the reattachment point upstream. For both models, the bounds obtained with a perturbation magnitude of 0.25 or larger encompass the DNS reattachment location. In addition, the DNS wall-shear stress is within the predicted bounds along most of the wavy wall.

An important observation is that the plots indicate a monotonic behavior in terms of the effect of the user-defined parameter values: an increase in the perturbation magnitude
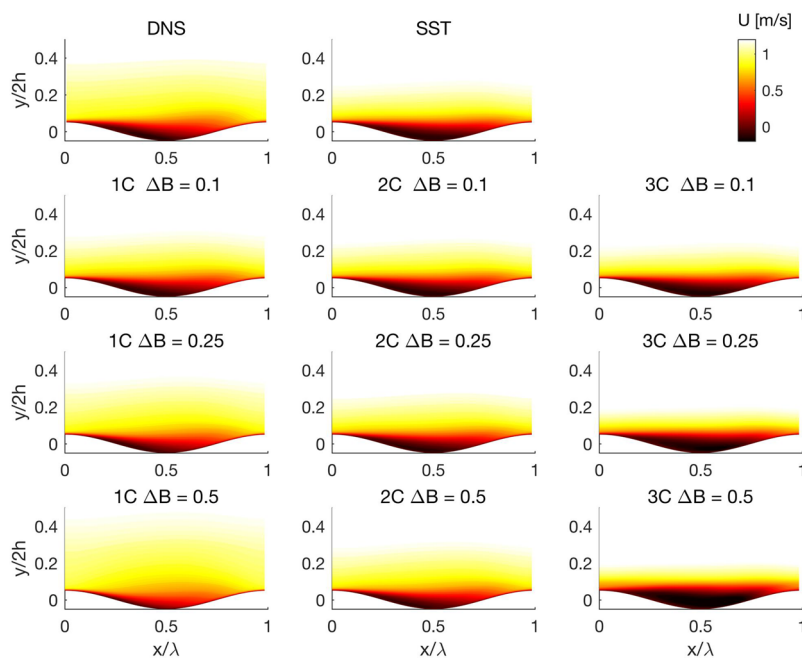

FIG. 8. Velocity contours for the wavy wall flow. DNS, SST $k - \omega$ baseline, and SST $k - \omega$ with different eigenvalue perturbation magnitudes for marker thresholds M2.
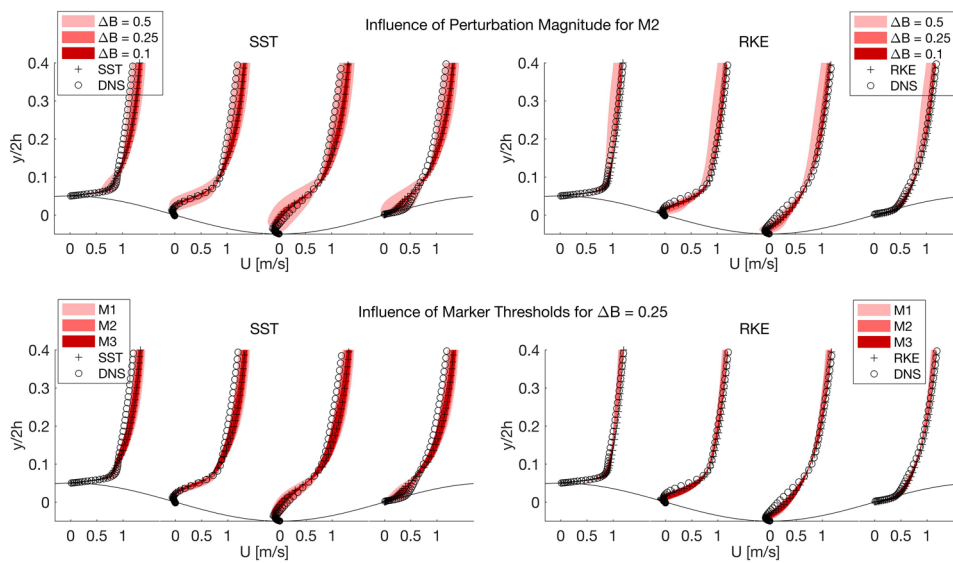
FIG. 9. Uncertainty intervals for the velocity profiles along the wavy wall at $x/\lambda = 0.0$, 0.25, 0.5, and 0.75.

or an increase in the area of the marked region both result in an increase in the bounds. This trend was found to be the same for all marker thresholds or perturbation sizes. The effect of the perturbation size is more pronounced than that of the marked region, which can be explained by the fact that the near-wall region is almost entirely marked for each set of marker thresholds.

B. Velocity field

Figure 8 presents the velocity contours from the DNS, baseline SST, and perturbed SST simulations with marker thresholds M2 and different perturbation magnitudes. In addition to showing the result for the 1C and 3C perturbation, we also present the result for the 2C perturbation. We note that the velocity contours for the RKE model showed similar observations but are omitted for brevity.

The contours confirm the behavior observed in the prediction of the wall shear stress. First, decreasing P_k increases the length of the separation region, while increasing P_k decreases separation. Second, the bounds predicted for the velocity field increase monotonically when the perturbation magnitude is increased. This monotonic increase also holds when increasing the area of the marked region, but the differences are more subtle and tend to manifest themselves locally in newly marked areas. The corresponding contour plots are omitted for brevity. A final observation is that perturbations to the 2C corner, which will result in a value for P_k in between the 1C and 3C perturbations, produce a result that lies in between these simulations.

To further quantify the above analysis of the velocity field, Fig. 9 presents line plots of velocity profiles at four locations along the wave crest. Similar to Fig. 7, each plot includes the values from the DNS, a baseline RANS simulation (SST on the left, RKE on the right), and three sets of bounds, obtained from

simulations with perturbations toward the one-component and three-component corner. In the upper row, the three different bounds reflect the effect of the perturbation magnitude ΔB, shown for M2. The lower row demonstrates the effect of the extent of the marked region, shown for $\Delta B = 0.25$. The plots further confirm that the bounds increase monotonically when increasing the perturbation size or marked region. The results indicate that the larger perturbation magnitude of $\Delta B = 0.5$ is required to provide bounds that encompass the DNS data for the velocity field.

V. ASKERVEIN HILL RESULTS AND DISCUSSION

In this section, we present the results obtained for the prediction of the FSR over Askervein Hill using the SST turbulence model. Based on the wavy wall results, we selected the marker thresholds corresponding to M2 in Table I. For the perturbation magnitude, we used $\Delta B = 0.5$ when introducing perturbations toward the 1C corner and $\Delta B = 0.1$ when introducing perturbations toward the 3C corner. The smaller perturbation toward the 3C corner was selected to ensure convergence of the results; the wavy wall results also indicated that the perturbations to the isotropic corner consistently produce results that are further from the reference solution. The final result is presented as a single uncertainty
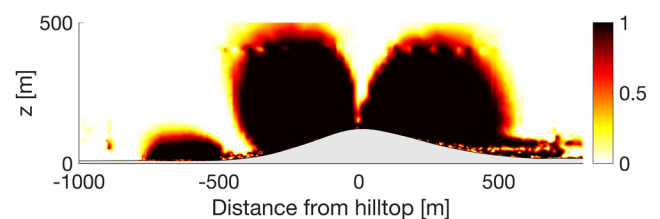

FIG. 10. Switch function for marker thresholds M2 on a vertical plane along line A over Askervein Hill.
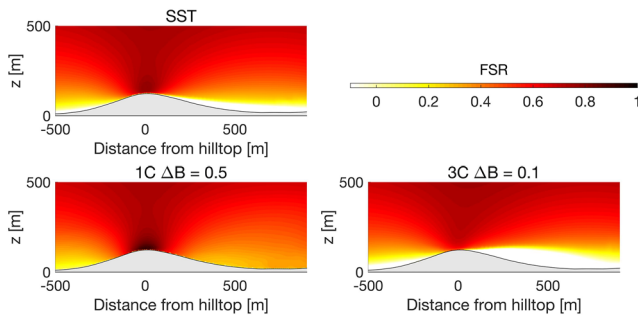
FIG. 11. Contours of fractional speed-up ratio on a vertical plane along line A over Askervein hill for the SST baseline simulation and for SST simulations with 1C and 3C eigenvalue perturbations.

interval for the baseline SST prediction and compared to the available field measurements. An investigation of the effect of these user-defined parameters can be found in Ref. 34 and was shown to lead to the same conclusions as those presented in Sec. IV.

Figure 10 presents the marker values on a vertical plane along line A (see Fig. 2), indicating how the marker identifies the flow regions surrounding the hill top. Figure 11 shows the contour plots of the fractional speed-up ratio (FSR) for the baseline and both perturbed simulations. As before, increasing the turbulence production using 1C perturbations results in a decrease of the extent of the separated region, while decreasing the production results in a larger separation bubble.

Figure 12 shows the corresponding uncertainty intervals for the FSR at 10 m height along lines A, AA, and B, respectively, and compares the results to the field measurement data. The uncertainty intervals encompass the majority of the experimental data points. As one would expect, the intervals are larger in the area downstream of the hill top (lines A and AA) where separation occurs, but there is limited experimental data available for comparison in this region. Along line B, which runs along the hill top almost perpendicular to the wind

direction, the uncertainty interval provides an adequate representation of the discrepancies between the field measurements and simulations. This indicates that turbulence model form uncertainties could at least partially be responsible for the previously described discrepancies in the FSR predictions near the hill top.

VI. CONCLUSIONS

The goal of the present study was to improve our understanding of a physics-based method to quantify turbulence model-form uncertainty in RANS predictions of separated flows over streamlined surfaces. Two different linear eddy-viscosity models, the SST $k - \omega$ model and the realizable $k - \epsilon$ model, were considered. The methodology is based on the framework presented in the study by Emory, Pecnik, and Iaccarino[30] and consists in introducing perturbations in the Reynolds stress tensor computed by the model and used in the momentum equations. The perturbations are defined in terms of a decomposition of the Reynolds stress tensor, i.e., its magnitude and the eigenvalue decomposition of the normalized anisotropy tensor.

We presented analyses to support the definition of the perturbation functions for these quantities. First, an *a priori* analysis indicated the dominant influence of the turbulence production term on the prediction of the Reynolds stress magnitude. Second, we showed that turbulence production is maximized when keeping the Reynolds stress eigenvectors aligned with the rate of strain tensor eigenvectors and introducing eigenvalue perturbations toward the one-component corner of the barycentric map, while it is reduced to zero when introducing eigenvalue perturbations toward the three-component (isotropic) corner of the map. Hence, the perturbation functions are defined to keep the original linear eddy-viscosity model orientation of the eigenvectors and perturb the eigenvalues to either the one-component or the three-component corner of the barycentric map. Subsequently, the updated anisotropy tensor is used to calculate the turbulence production term in the transport equation for the turbulence kinetic energy, thereby affecting the magnitude of the Reynolds stress tensor. The method
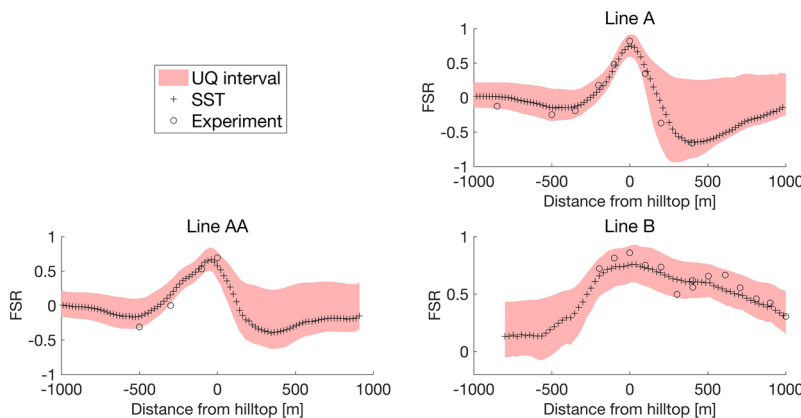

FIG. 12. Comparison of fractional speed-up ratio along lines A, AA, and B over Askervein hill from the baseline SST simulation and the field experiment, with uncertainty intervals from two (1C and 3C) perturbed simulations.

uses two user-defined parameters: (1) a marker threshold, which identifies the spatial extent of the perturbed region, and (2) a perturbation size, which specifies the magnitude of the displacement toward the corners of the barycentric map.

Results for both the wavy wall flow and the flow over Askervein hill indicate that the perturbations that increase P_k decrease the extent of the separation region, while perturbations that decrease P_k increase the region of separated flow. In both cases, the resulting bounds on the velocity field can successfully encompass the DNS or experimental data, provided the extent of the perturbed region and the perturbation sizes are sufficiently large. Importantly, we observed a monotonic behavior of the magnitude of the predicted bounds as a function of the two user-defined parameters; such monotonic behavior is imperative for a method that aims to predict plausible bounds for quantities of interest. It also indicates that imposing eigenvalue perturbations toward the corners of the barycentric map in the entire flow domain would consistently provide conservative bounds on predictions of separated flows over streamlined surfaces. This could provide useful prior information for more complex methods that consider, for example, spatial variability in the perturbations.

Future work will focus on analyzing the capability of the method to capture uncertainty in the modeled turbulence quantities; this will, for example, be relevant for modeling turbulent dispersion. In addition, we will investigate the performance of the method in different configurations, including bluff body flows.

REFERENCES

[1]S. Cheung, T. A. Oliver, E. Prudencio, S. Prudhomme, and R. D. Moser, "Bayesian uncertainty analysis with applications to turbulence modeling," Reliab. Eng. Syst. Saf. **96**, 1137–1149 (2011).

[2]E. Dow and Q. Wang, "Quantification of structural uncertainties in the k – ω turbulence model," AIAA Paper 2011-1762, 2011.

[3]M. Ming, J. Lu, and G. Tryggvason, "Using statistical learning to close two-fluid multiphase flow equations for a simple bubbly system," Phys. Rev. Fluids **27**, 092101 (2015).

[4]J.-L. Wu, J.-X. Wang, and H. Xiao, "A Bayesian calibration-prediction method for reducing model-form uncertainties with application in RANS simulations," Flow, Turbul. Combust. **97**, 761–786 (2016).

[5]J. Ling and J. Templeton, "Evaluation of machine learning algorithms for prediction of regions of high reynolds averaged Navier-Stokes uncertainty," Phys. Fluids **27**, 085103 (2015).

[6]E. J. Parish and K. Duraisamy, "A paradigm for data-driven predictive modeling using field inversion and machine learning," J. Comput. Phys. **305**, 758–774 (2016).

[7]A. P. Singh and K. Duraisamy, "Using field inversion to quantify functional errors in turbulence closures," Phys. Fluids **28**, 045110 (2016).

[8]H. Xiao, J.-X. Wang, and R. G. Ghanem, "A random matrix approach for quantifying model-form uncertainties in turbulence modeling," Comput. Methods Appl. Mech. Eng. **313**, 941–965 (2017).

[9]J.-X. Wang, J.-L. Wu, and H. Xiao, "Physics-informed machine learning approach for reconstructing reynolds stress modeling discrepancies based on dns data," Phys. Rev. Fluids **2**, 034603 (2017).

[10]K. Duraisamy, G. Iaccarino, and H. Xiao, "Turbulence modeling in the age of data," Annu. Rev. Fluid Mech. **51**, 357–377 (2019).

[11]M. Emory, J. Larsson, and G. Iaccarino, "Modeling of structural uncertainties in Reynolds-averaged Navier-Stokes closures," Phys. Fluids **25**, 110822 (2013).

[12]C. Gorlé and G. Iaccarino, "A framework for epistemic uncertainty quantification of turbulent scalar flux models for Reynolds-averaged Navier-Stokes simulations," Phys. Fluids **25**, 055105 (2013).

[13]C. Gorlé, M. Emory, J. Larsson, and G. Iaccarino, "Epistemic uncertainty quantification for RANS modeling of the flow over a wavy wall," in *Annual Research Briefs 2012* (Center for Turbulence Research, Stanford, CA, 2012), pp. 81–91.

[14]G. Iaccarino, A. Mishra, and S. Ghili, "Eigenspace perturbations for uncertainty estimation of single-point turbulence closures," Phys. Rev. Fluids **2**, 024605 (2017).

[15]R. Rossi, "A numerical study of algebraic flux models for heat and mass transport simulation in complex flows," Int. J. Heat Mass Transfer **53**, 4511–4524 (2011).

[16]P. Taylor, H. Teunissen, and CMSR Branch, *The Askervein Hill Project: Report on the September/October 1983, Main Field Experiment*, Internal Report MSRB (Meteorological Services Research Branch, Atmospheric Environment Service, 1985).

[17]H. W. Teunissen, M. E. Shokr, A. J. Bowen, C. J. Wood, and D. W. R. Green, "The Askervein hill project: Wind-tunnel simulations at three length scales," Boundary-Layer Meteorol. **40**, 1–29 (1987).

[18]H. C. Chen and V. C. Patel, "Near-wall turbulence models for complex flows including separation," AIAA J. **26**, 641–648 (1988).

[19]C. Rhie and W. Chow, "Numerical study of the turbulent flow past an airfoil with trailing edge separation," AIAA J. **21**, 1525–1532 (1983).

[20]J. H. Ferziger and M. Peric, *Computational Methods for Fluid Dynamics* (Springer Science & Business Media, 2012).

[21]R. Rossi, "Passive scalar transport in turbulent flows over a wavy wall," Ph.D. thesis, Università degli Studi di Bologna, 2006.

[22]G. Raithby, G. Stubley, and P. Taylor, "The Askervein hill project: A finite control volume prediction of three-dimensional flows over the hill," Boundary-Layer Meteorol. **39**, 247–267 (1987).

[23]F. A. Castro, J. Palma, and A. S. Lopes, "Simulation of the Askervein flow. Part 1: Reynolds averaged Navier-Stokes equations (k-ε turbulence model)," Boundary-Layer Meteorol. **107**, 501–530 (2003).

[24]H.-G. Kim and V. Patel, "Test of turbulence models for wind flow over terrain with separation and recirculation," Boundary-Layer Meteorol. **94**, 5–21 (2000).

[25]H. G. Kim, V. Patel, and C. M. Lee, "Numerical simulation of wind flow over hilly terrain," J. Wind Eng. Ind. Aerodyn. **87**, 45–60 (2000).

[26]O. Undheim, H. Andersson, and E. Berge, "Non-linear, microscale modelling of the flow over Askervein hill," Boundary-Layer Meteorol. **120**, 477–495 (2006).

[27]A. Paci, "CFD sensitivity study for the flow field around Askervein hill," M.S. thesis, University of Liege, 2016.

[28]P. Richards and R. Hoxey, "Appropriate boundary conditions for computational wind engineering models using the k-ε turbulence model," J. Wind Eng. Ind. Aerodyn. **46-47**, 145–153 (1993).

[29]A. Parente, C. Gorlé, J. van Beeck, and C. Benocci, "A comprehensive modelling approach for the neutral atmospheric boundary layer: Consistent inflow conditions, wall function and turbulence model," Boundary-Layer Meteorol. **140**, 411–428 (2011).

[30]M. Emory, R. Pecnik, and G. Iaccarino, "Modeling structural uncertainties in Reynolds-averaged computations of shock/boundary layer interactions," AIAA Paper 2011-0479, 2011.

[31]S. Banerjee, R. Krahl, F. Durst, and C. Zenger, "Presentation of anisotropy properties of turbulence, invariants versus eigenvalue approaches," J. Turbul. **8**, N32 (2007).

[32]A. Liberzon, B. Luthi, W. Kinzelbach, and A. Tsinober, "Experimental study of the structure of flow regions with negative turbulent kinetic energy production in confined three-dimensional shear flows with and without buoyancy," Phys. Fluids **17**, 095110 (2005).

[33]C. Gorlé, J. Larsson, M. Emory, and G. Iaccarino, "The deviation of parallel shear flow as an indicator of linear eddy-viscosity model inaccuracy," Phys. Fluids **26**, 051702 (2014).

[34]S. Zeoli, "Numerical simulation of flows with application to wind engineering problems," Ph.D. thesis, University of Mons, 2018.